CHEMISTRY OF MATERIALS

pubs.acs.org/cm

Article

Li_2O Solid Electrolyte Interphase: Probing Transport Properties at the Chemical Potential of Lithium

Rui Guo and Betar M. Gallant*

Cite This: Chem. Mater. 2020, 32, 5525−5533

Read Online

ACCESS | Metrics & More | Article Recommendations | Supporting Information

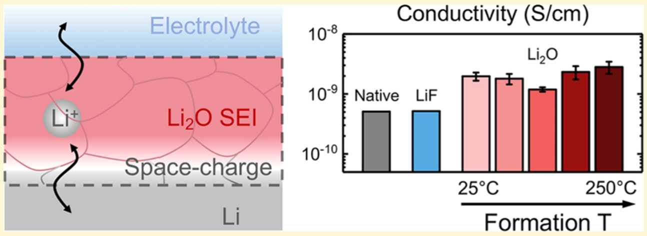

ABSTRACT: Lithium (Li) anodes suffer from numerous challenges arising from the chemically inhomogeneous nature of the native solid electrolyte interphase (SEI), which impedes smooth plating and leads to dendrite growth. In spite of much attention given of late to engineering Li interfaces, there is still limited understanding of the desired chemical composition of an improved Li SEI. One major challenge has been the lack of empirical data on the structure−property−performance relations in individual SEI phases, specifically those present at the metallic Li interface, where the chemical potential imposed by Li will yield different material properties than the bulk analogues typically invoked to understand the SEI behavior. Herein, we report the preparation of single-component SEIs of lithium oxide (Li_2O) grown *ex situ* on Li foils by controlled metal−gas reactions, generating "deconstructed" model interfaces with a nanoscale thickness (20−100 nm) similar to the native, yet more complex multiphasic SEI. The model Li|Li_2O electrodes serve as a platform for further chemical and electrochemical characterization. In particular, electrochemical impedance spectroscopy, combined with interface modeling, is used to extract transport properties (ionic conductivity, diffusivity, charge carrier concentration, and activation energy barriers) of Li|Li_2O in symmetric cells with EC/DEC electrolytes. The Li_2O SEI is further studied as a function of a synthesis condition, revealing microstructural sensitivities that can be tuned to modulate transport behaviors. Finally, results are compared with single-phase Li|LiF interfaces synthesized herein and with the native SEI to isolate chemistry- and structure-specific differences.

1. INTRODUCTION

Li metal is an attractive material for future high-energy-density batteries because of its large gravimetric capacity (3860 mA h/g_{Li} *vs* 372 mA h/$g_{graphite}$), combined with low negative electrochemical potential (−3.04 V *vs* SHE), unique among candidate anode materials.[1,2] However, the tendency toward dendritic growth has been a formidable issue, as dendrites not only induce capacity fade by consuming the electrolyte and creating dead Li[3] but also lead to intolerable safety issues such as short circuits.[4] Following numerous studies on the mechanism of roughened Li deposition and dendrite growth,[5,6] it is now generally accepted that the inhomogeneous nature of the solid electrolyte interphase (SEI)[7,8] underlies these issues. The native SEI is conventionally described as having a multiphasic structure containing fully reduced, dense ionic phases (*e.g.*, Li_2O and LiF) closest to the Li interface in the "inner layer", and lithium carbonate (Li_2CO_3), less-reduced semi-carbonates and organic Li salts (*e.g.*, CH_3OCO_2Li and CH_3CH_2OLi) comprising a porous "outer layer" closest to the electrolyte.[9] Although these phases are poor ionic conductors in bulk form, the nanoscale SEI thickness (tens of nm) permits Li^+ transport.[8] However, the chemically nonuniform native interface is readily compromised during Li cycling, leading to inhomogeneous deposition and breakdown of the fragile SEI.

To address these challenges, researchers have adopted two overarching approaches. The first has been to improve Li cyclability through the design of new electrolyte formulations including additives (*e.g.*, $LiNO_3$, fluoroethylene carbonate) or other highly fluorinated compounds.[10−13] Others conducted *ex situ* modification of Li foils, creating a so-called "artificial SEI" (*e.g.*, LiF, Li_3N, Al_2O_3, or MoS_2) which attempts to decouple Li from the electrolyte and thus reconceive the SEI chemistry.[14−18] Such Li modification strategies are still in early days, and the practical viability of such strategies has yet to be determined.

On the other hand, multiple studies have sought to develop improved fundamental understanding of the properties and function of individual phases within the native SEI. Efforts have focused predominantly on ionic SEI components (*i.e.*, LiF, Li_2O, and Li_2CO_3), which have been studied intensively by molecular dynamics (MD) simulations, density functional theory (DFT) calculations, as well as experimental conductivity measurements.[19−22] Chen *et al.*,[19] positing vacancies to be the majority carriers in the SEI, found by DFT that Li^+

Received: January 26, 2020
Revised: May 27, 2020
Published: May 28, 2020

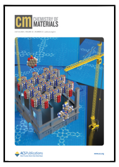

ACS Publications

https://dx.doi.org/10.1021/acs.chemmater.0c00333
Chem. Mater. 2020, 32, 5525−5533

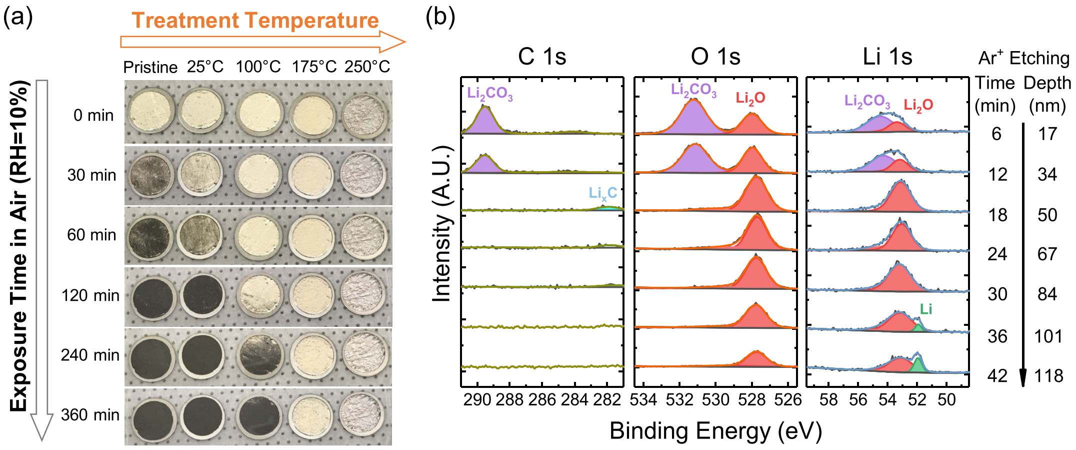

Figure 1. (a) Air-exposure experiment for pristine Li and for Li treated in pure O_2 gas for 1 h at temperatures ranging from 25 to 250 °C. (RH = relative humidity = 10%). (b) XPS depth profile of Li|Li_2O samples formed at 250 °C for 1 h.

diffusion in bulk Li_2O and Li_2CO_3 can be fast (migration energy barriers of 0.2−0.5 eV) under these assumptions. Benitez and Seminario[20] found by MD simulations that the predominant diffusion mechanisms are direct ion-exchange in Li_2O, and vacancy-assisted and knock-off diffusion in LiF and Li_2CO_3. Lorger *et al.*[21] also invoked vacancies as the charge carriers in bulk crystalline Li_2O based on sintered pellet measurements, but found that the measured ionic conductivities did not match well with those of typical SEI layers in Li cells. Possible effects of grain boundaries have also been investigated in these phases.[22,23] However, fewer studies have investigated the SEI integrated onto Li metal. Given the experimental challenges, most efforts have been computational.[24−26] Shi *et al.*[24] found that the dominant charge carriers of crystalline Li_2CO_3 at potentials close to Li metal are not Li^+ vacancies, which predominate at higher potentials, but rather interstitials, which migrate *via* a knock-off mechanism with diffusivity as high as $D = 1.1 \times 10^{-7}$ cm^2/s. Meanwhile, Yildirim *et al.*[25] found by DFT that the predominant charge carriers in LiF are Li^+ vacancies in the potential range 0−4 V versus Li/Li^+, although it was noted that a knock-off mechanism of Li^+ interstitials could provide a much faster migration pathway if available. Overall, while the understanding of model interfaces has progressed substantially, a unified understanding of the SEI function, and especially transport, has yet to emerge, given varying assumptions and approaches taken to describe the Li interface.

In this context, this work seeks to provide new experimental insight into transport within the Li SEI, and specifically, into the contributions of individual ionic phases omnipresent at such interfaces with a particular emphasis on Li_2O. Although Li_2O has been extensively studied as a bulk material, for example, as sintered pellets, single crystals, or bulk powders, and characterized electrochemically in bulk by electrochemical impedance spectroscopy (EIS) or solid state nuclear magnetic resonance measurements,[21,27−32] the microstructure, ionic, and chemical properties of such materials may not adequately describe those occurring in an SEI on Li, with vastly different chemical potentials. To address this issue, we herein report the synthesis and characterization of all-Li_2O SEIs grown directly on Li by the O_2 gas treatment of Li foils under moderate reaction conditions (25−250 °C). The resulting interfaces are thin (20−100 nm) and conformal to Li, serving as an appropriate model to study a "deconstructed" SEI with Li_2O as the sole component. Ionic conductivity, charge carrier concentration, and carrier diffusivity within the Li_2O interface are measured *in situ* by analyzing EIS data based on an appropriate underlying physical model of the interface.[33,34] Results are also compared with similarly formed Li|LiF interfaces synthesized using a fluorinated gas reactant.[35] As much as three orders-of-magnitude difference in ionic conductivity is observed between the single-component Li_2O SEI (~10^{-9} S/cm) and that of sintered bulk Li_2O pellets reported in the literature[21] (~10^{-12} S/cm) at room temperature, underscoring the conclusion that Li-derived interphases present in actual battery environments differ significantly from their bulk counterparts.

2. EXPERIMENTAL METHODS

2.1. Synthesis of Li_2O or LiF Interfaces on Li. All handling of Li electrodes was conducted in an Ar-filled glove box (MBraun) with O_2 and H_2O contamination below 0.1 ppm. The Li foil (≥99.9%, Alfa Aesar) was mechanically polished using an electric grinder with an aluminum oxide grinding tip (Dremel), then rolled and punched to circles of 15 mm diameter. Punched foils were then loaded into a home-made stainless-steel reaction vessel (Kurt J. Lesker Co.) and purged with ultrapure O_2 (99.999%, Airgas, for Li_2O) or NF_3 (99.999%, Electronic Fluorocarbons, LLC, for LiF) within the glove box. The vessel was then pressurized to a gauge pressure of 240 kPa before being sealed and transferred to a thermal chamber held at the target treatment temperature (25−250 °C). After treatment (1−24 h), the reaction vessel was opened under active vacuum and all gases were removed before being transferred directly back to the Ar glove box. Note that the LiF film thickness (~50 nm) was slightly higher than in our previous report,[35] where the metal−gas reaction was conducted on a hot plate, due to slight differences in heating and thus the reaction environment.

2.2. Electrochemical Measurements. Symmetric Li−Li cells, in which both electrodes were modified by Li_2O or LiF as indicated, were assembled in 2032-type coin cells with one piece of the Celgard 2325 separator [previously dried in a vacuum oven (Buchi Corp.) at 65 °C for 12 h] and 20 μL of the electrolyte (1.0 M $LiPF_6$ in EC/DEC, v/v = 1/1, used as received from Sigma-Aldrich). EIS measurements were conducted on a Biologic VMP3 system with a frequency range of 1 MHz to 10 mHz. EIS fitting was conducted using EC-Lab Zfit software and was fit over the frequency range of 20 kHz to approximately 20 Hz, the lower bound of which varied from cell-to-cell because of the overlap of the secondary arc in the low-frequency region. Error bars for EIS measurements in Figure 3c reflect standard deviations calculated from 3 to 6 cells. The sensitivity of the

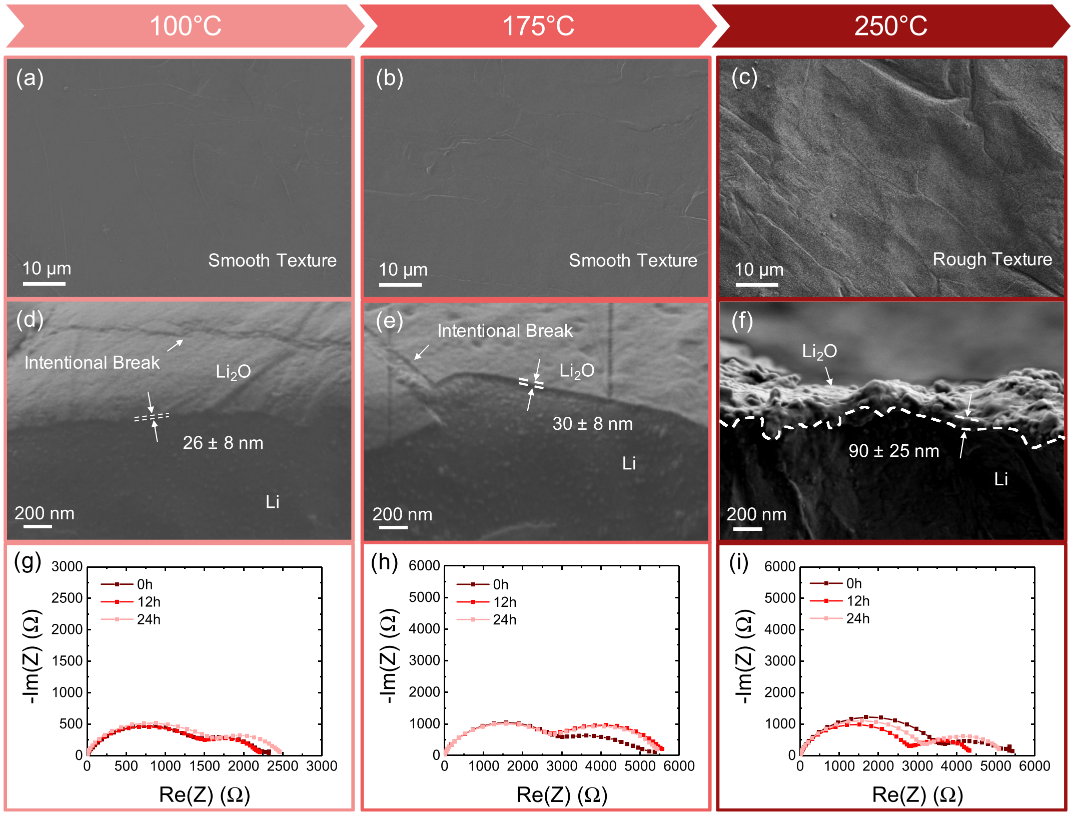

Figure 2. (a–c) Top view and (d–f) cross-section view of SEM images of Li|Li_2O prepared at (a,d) 100, (b,e) 175, and (c,f) 250 °C for 1 h. (g–i) Nyquist plots of symmetric coin cells of Li|Li_2O prepared at (g) 100, (h) 175, and (i) 250 °C for 1 h. The electrolyte was 1 M $LiPF_6$ EC/DEC (v/v = 1/1).

EIS fitting and the transport properties derived from the fitting results are summarized in the Supporting Information.

2.3. Film Characterization. Scanning electron microscopy (SEM) images were taken with a Zeiss Merlin scanning electron microscope at an accelerating voltage of 1 kV. Samples were transferred to the SEM without exposure to air *via* a transfer vessel (Semilab Inc.) built for the Zeiss SEM airlock. Error bars for the SEM-determined thickness in Figure 3c were determined from measurements at three random positions on the edges of the cross-section views in Figure 2d–f. X-ray photoelectron spectroscopy (XPS) analysis was conducted on a PHI VersaProbe II X-ray Photoelectron Spectrometer equipped with a floating voltage Ar single-ion gun for depth profiling. Samples were transferred to XPS in an air-sensitive transfer vessel to minimize exposure to air. Binding energies were calibrated by the adventitious carbon peak at 284.8 eV.[36] Ar-ion sputtering for XPS depth profiling was carried out at a beam acceleration of 2 kV and current of 2 μA over an area of 2 mm × 2 mm. The sputtering rate calibrated separately on a SiO_2 surface was ~2.8 nm/min. Error bars for XPS depth profiles in Figure 3c were determined based on uncertainty in etching time intervals.

3. RESULTS AND DISCUSSIONS

3.1. Characterization of the Li_2O SEI Prepared by Metal–Gas Reaction.

To fabricate a single-component SEI grown directly on Li, Li foils were reacted in O_2 gas at fixed temperature ranging from 25 to 250 °C for 1 h, forming a compact layer of Li_2O.[37−39] Air-exposure of post-reacted Li (Figure 1a) indicated the protective effect of the formed Li_2O surface layer. When exposed to the ambient environment with relative humidity of 10%, pristine Li tarnished immediately and blackened fully over 30 min. In contrast, the Li pretreated by O_2 showed outcomes that depended on the treatment conditions. Li foils treated at 25 °C (1 h) exhibited similar air reactivity as pristine Li, indicating minimal quantities of imparted Li_2O; in contrast, those treated at higher temperatures showed impeded (at 100 °C) or no (at 175 or 250 °C) air reactivity, indicating the formation of a Li_2O interface with sufficient coverage. Li surfaces showed significant roughness after treatment at 250 °C (1 h) that was visible to the eye, which was caused by the melting and resolidification of the Li metal (T_m = 180.5 °C) underneath the Li_2O surface layer. Longer treatment times at lower temperatures (*e.g.*, 24 h at 175 °C) also showed excessively thick Li_2O layers (>500 nm, Figure S1). Thus, all further samples utilized 1 h reaction time for further studies.

XPS depth profiling by Ar-ion etching (Figure 1b) confirmed that the major component of the surface of treated Li (O_2, 250 °C for 1 h) was Li_2O. The etching rate was calibrated separately to be ~2.8 nm/min using a 50 nm thick SiO_2 layer on a Si wafer. Some quantities of Li_2CO_3, as indicated by peaks in the O 1s (531.4 eV) and C 1s (289.8 eV) spectra,[40] were observed in the outer-most layers but were removed after 12 min of Ar-ion sputtering and are attributable to trace contamination during sample transfer as they were not found within the bulk of the film. The remaining O 1s peak at 528.0 eV and Li 1s peak at 53.3 eV indicated the presence of Li_2O throughout the layer.[40] Following top-surface removal, the C 1s peak was negligible, showing only minor amounts of lithium carbide species (282.2 eV)[9] because of the reaction with trace C formed during etching. After 36 min, the metallic Li^0 peak emerged at 52.1 eV,[40] from which the Li_2O thickness was determined: 25–30 nm for reactions between 25 and 175 °C, and ~100 nm at 250 °C. Similar XPS depth profiles were observed for other reaction conditions (Figure S2a).

Top-view SEM images (Figure 2a−c) indicated that the Li_2O SEI surface was smooth and conformal when formed below the melting point of the Li metal. However, in agreement with optical images (Figure 1a), significant roughening occurred at higher temperature (250 °C, Figure 2c). Regardless, no cracks at micrometer scale were identified. Meanwhile, tilted cross-sectional SEM images (Figure 2d−f) showed the presence of the imparted Li_2O layers as a function of reaction temperature (thickness measurements were made by intentionally breaking the sample to expose underlying Li). For samples treated at 100 and 175 °C, Li_2O films were visually estimated to be 26 ± 8 and 30 ± 8 nm from Figure 2d,e, respectively. A thicker Li_2O film, 90 ± 25 nm, was observed for Li treated at 250 °C (Figure 2f). Excellent agreement was found between SEM-determined thicknesses and those estimated from XPS depth profiles. Therefore, the modified interfaces—conformal, single-phase, with reasonable thickness (tens of nm) on the scale of the native SEI—are appropriate to serve as model $Li|Li_2O$ interfaces for subsequent characterization.

EIS experiments were next carried out in symmetric coin cells consisting of two pretreated $Li|Li_2O$ electrodes over the first 24 h post-cell assembly (Figure 2g−i). All measurements were conducted at open circuit. The electrolyte was a conventional carbonate electrolyte, 1 M $LiPF_6$ EC/DEC (v/v = 1/1). For all synthesis temperatures, the impedance spectra of $Li|Li_2O$ cells exhibited two distinct semicircles. The semicircle comprising the high-frequency range (100 kHz to 20 Hz) is typically attributed to charge transfer through the denser, inner (ionic) layer of the SEI,[41,42] while a semicircle comprising the lower frequency range (10 Hz to 10 mHz) has been attributed to the porous outer layer comprising the interface between the SEI and electrolyte[43,44] (EIS of untreated Li with a native SEI is included for comparison in Figure S3). Although the presence of an outer layer on the Li_2O SEI was initially unexpected, a recent study by Kamphaus *et al.*[26] utilized AIMD simulations to model the SEI−electrolyte interface and found that the electrolyte could decompose or react with an Li_2O SEI layer. In addition, Aurbach[45] suggested that Li_2O can be nucleophilic toward the carbonate electrolyte. Thus, we postulated that the second semicircle observed herein can be explained by the reaction of the outermost interface of Li_2O with the electrolyte upon soaking, creating a distinct outer layer, likely porous, in addition to the Li_2O inner layer. To investigate this, XPS depth-profiling analysis was conducted on the nominally all-Li_2O SEI after being soaked in the electrolyte for 20 h and compared with that of the as-prepared Li_2O sample (Figure S2). The results confirm that the Li_2O surface underwent some chemical changes at the outer region of the SEI, as indicated by the presence of LiF (Figure S2b). The penetration depth of this chemical change was, however, limited in depth to approximately the top ∼10 nm. Consequently, all analysis of EIS results were applied to the high-frequency semicircle, which was interpreted to correspond to the remaining underlying Li_2O. The complex nature of the buried ionic/outer-layer interface and dynamic chemical reactivity of the SEI requires further work to be elucidated in full, and is planned as a subject of future studies.

The Li_2O SEI prepared at 100 °C showed relatively stable impedance over the first 12 h following cell assembly (Figure 2g), with a small increase in both high- and low-frequency arcs after 24 h, indicating that Li was not fully protected by Li_2O in agreement with the air-exposure experiments. In contrast, the Li_2O SEI formed at 175 °C was more stable over 24 h, with slight changes in the low-frequency region between 0 and 12 h (Figure 2h), possibly due to as-described reactions at the outer SEI−electrolyte interface. The EIS results of Li_2O formed at 250 °C exhibited the largest variations during resting (Figure 2i), suggesting higher reactivity at the interface of the SEI and electrolyte because of its rougher surface morphology.

3.2. Equivalent Circuit and Physical Model of the SEI.

Previously, Zaban *et al.*[44] proposed a model consisting of five series RC circuits to describe the multilayer nature of the native SEI in both carbonate- and ether-based electrolytes, where five was the minimum number necessary to achieve adequate fitting. Peled *et al.*[23] further considered contributions of grain boundaries of each sublayer to the overall SEI impedance, which necessitated a cautious examination of the physical meaning of each RC circuit in the SEI model. Given different proposed models in the literature, Churikov *et al.*[33,34] compared multiple equivalent circuit options, and developed a relatively simple model for the charge transfer process of the SEI based on empirical analysis. The proposed model consisted of only one bulk SEI layer with a space-charge region at the metal−SEI interface and also accounted for the diffusion of ionic charge carriers in the vicinity of the space-charge region. The results could achieve an excellent fit to the EIS data using an equivalent circuit containing only four elements (*vs* 10−15 in previous models), helping to avoid potentially ambiguous fitting results, overfitting, or uncertain physical meanings.

We adopted this model to describe the physical behavior and transport within the solid-state Li_2O interface on Li, and specifically, within the higher-frequency arc corresponding to the compact inner layer in agreement with our EIS (Figure 2g−i) and XPS results (Figure S2). A schematic of the SEI model and corresponding equivalent circuit are shown in Figure 3a. Given the differences in chemical potentials (Fermi levels) of Li and Li_2O, a space-charge region forms at their

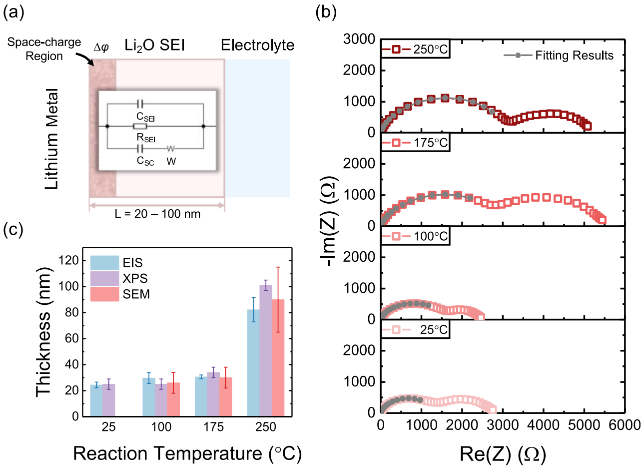

Figure 3. (a) SEI equivalent circuit model for a single $Li|Li_2O$ electrode (full cell equivalent circuit is shown in the Supporting Information). $\Delta\varphi$ is the potential drop across the space-charge region. (b) Nyquist plots of the EIS data and the fitting results for symmetric coin cells of $Li|Li_2O$ electrodes. (c) Summary of estimated thicknesses of the Li_2O SEI layers obtained by three different methods: SEM imaging; XPS sputtering; and as a direct output of the impedance model; error bars are described in the Experimental Methods. The electrolyte used in all cells is 1 M $LiPF_6$ EC/DEC (v/v = 1/1).

junction because of the mutual diffusion of charge carriers required to align interfacial energy levels.[26,34] This space-charge layer can be modeled as having a distinct differential capacitance, C_{SC}, and a thickness characterized by the Debye length, L_D, provided that the Debye length is smaller than the total Li_2O thickness, which was verified in the following modeling results and listed in Table S1. Three additional elements are included to describe transport through the Li_2O layer: (i) a geometric capacitance of the Li_2O SEI, C_{SEI}; (ii) an ionic resistance, R_{SEI}; and (iii) a Warburg element, Z_W, included to capture the solid-state diffusion of charge carriers in the vicinity of the space-charge region. Therefore, the equivalent circuit of a symmetric coin cell is composed of one electrolyte resistance and two identical SEI circuits in series (Figure S4), further simplified into Figure S5 for the purpose of data fitting. To accurately capture the intrinsic behavior of Li_2O, the fitting was performed in the high-mid frequency range (20 kHz to 20 Hz) but omitted the low-frequency semicircle related to the porous outer layer, as described above. The corresponding fitting results using the above model showed excellent agreement with the EIS data (Figures 3b and S6).

Physicochemical properties of the SEI were next determined by deconstructing the expressions of the equivalent circuit elements.[34] With C_{SEI} and R_{SEI} acquired numerically from the fitting, the SEI thickness L and ionic conductivity σ_0 were determined from the following expressions relevant for a planar electrode

$$C_{SEI} = \frac{\varepsilon\varepsilon_0 A}{L} \quad (1)$$

$$R_{SEI} = \frac{L}{\sigma_0 A} \quad (2)$$

where ε_0 and ε are the vacuum permittivity and the relative permittivity (dielectric constant), respectively ($\varepsilon_{Li_2O} = 8.9$, $\varepsilon_{LiF} = 9.0$),[33,46] and A is the known electrode area ($A = 1.77$ cm^2). The Warburg impedance for the charge carrier diffusion is $Z_W = \frac{\sqrt{2}W}{\sqrt{i\omega}}$, where ω is the angular frequency and the Warburg constant W is defined as

$$W = \frac{k_B T}{q^2 n_0 \sqrt{2D}A} \quad (3)$$

k_B is the Boltzmann constant, T is measurement temperature, q is the elementary charge, n_0 and D are the concentration and diffusivity of the charge carriers in the SEI, respectively (note that no assumptions are made as to the nature of charge carriers; see additional discussion below). The two unknowns, n_0 and D, are determined by the Warburg constant in eq 3 along with the Nernst−Einstein relationship for mobility, μ

$$\mu = \frac{\sigma_0}{qn_0} = \frac{q}{k_B T}D \quad (4)$$

Following determination of L, σ_0, n_0, and D, the Debye length L_D can be therefore calculated by taking the charge carrier concentration n_0 into eq 5

$$L_D = \sqrt{\frac{\varepsilon\varepsilon_0 k_B T}{2q^2 n_0}} \quad (5)$$

To validate the fitting results, the thicknesses of the SEI layers, the output of eq 1, were compared with measurements of thickness mentioned previously, that is, XPS depth profiles (Figure 1b) and SEM images (Figure 2d−f), and showed excellent agreement (Figure 3c). Specifically, the fittings indicated an SEI thickness increasing from 20 to 30 nm at reaction temperatures increasing from 25 to 175 °C and reaching ∼90 nm at 250 °C, which is highly consistent with experiments. The sensitivity of EIS measurements and the fitting process to the physicochemical properties of the SEI layers are also shown in Figures S7 and S8, respectively; overall trends were found to be highly robust to uncertainty in assumed physical parameters (A, ε) up to ±50% examined here.

3.3. Measured Transport Parameters in Single-Phase SEIs.

The analysis was next extended to quantify transport parameters as a function of Li_2O formation temperature. Note that in contrast to L, which is directly validated with the experiment, properties σ_0, D, and n_0 are coupled in eqs 2−4 and therefore cannot be determined interpedently, that is, from individual measurements of each parameter. Regardless of that, meaningful physical values and trends emerged (see the Discussion section). As shown in Figure 4, below the melting point T_m of Li metal, σ_0, D, and n_0 remained roughly constant (∼1 × 10^{-9} S/cm, 2 × 10^{-9} cm^2/s and 2 × 10^{-7} mol/cm^3, respectively). However, significant changes were observed above T_m. Specifically, σ_0 increased by threefold up to 3.5 × 10^{-9} S/cm; D increased from 2.0 × 10^{-9} up to 2.8 × 10^{-8} cm^2/s; and n_0 decreased significantly, from 1.5 × 10^{-7} to 2.6 × 10^{-8} mol/cm^3 between 175 and 250 °C. As discussed further below, the nature of charge carriers within the SEI is strongly dependent upon the chemical potential of the electrode, which is the same across these samples given the presence of Li;[24,25,47,48] therefore, these changes with different reaction temperatures are more likely to reflect changes in the Li_2O microstructure, rather than in the fundamental nature of ion transport in the films. Compared to a native SEI (∼6 to 10 nm from EIS) formed in the same carbonate electrolyte with multiple constituent phases, Li|Li_2O has significantly higher D

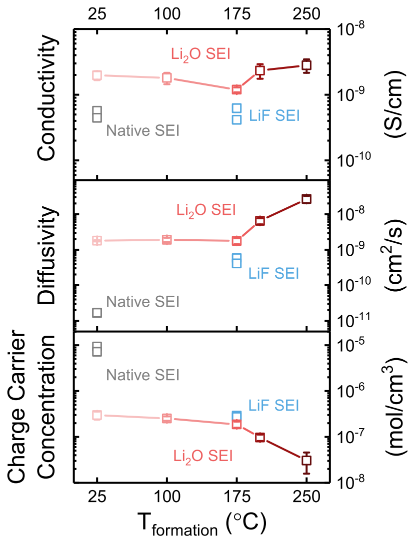

Figure 4. Conductivity, charge carrier diffusivity, and charge carrier concentration of the different SEI layers derived from the fitting results of the EIS data. The error bars for the Li_2O SEI are calculated from three data points. Two data points are shown for the native SEI and LiF SEI.

$(1.8 \times 10^{-9}$ *vs* 1.6×10^{-11} cm^2/s for native SEI) but lower n_0 $(1.8 \times 10^{-7}$ *vs* 8.5×10^{-6} mol/cm^3, respectively), resulting in an overall higher conductivity ($\sigma_0 = 5.1 \times 10^{-10}$ S/cm for the native SEI).

Analogous studies were also conducted on an all-LiF SEI grown on Li foils using a metal-gas reaction with NF_3 reported previously.[35] The thickness of the LiF SEI formed at 175 °C was found to be ~25 nm by EIS fitting, similar to the thickness of the Li_2O SEI formed at the same temperature in O_2 (~29 nm). σ_0 of LiF was around 5.2×10^{-10} S/cm (Figure 4), approximately half of the conductivity of Li_2O and more similar to the conductivity of the native SEI. n_0 of both the LiF and Li_2O SEI were similar. However, D in the LiF SEI (about 4.5×10^{-10} cm^2/s) was lower than that of Li_2O, which accounted for the overall lower conductivity of LiF.

Transport properties of the Li_2O and LiF SEI were also investigated as a function of applied temperature in the range 9−65 °C. Figures 5a,b and S9 show temperature-dependent EIS data of symmetric cells using either Li|Li_2O or Li|LiF electrodes with interfaces formed at 175 °C for 1 h. The resistance of the high-frequency semicircle corresponding to the ionic Li_2O or LiF layer decreased significantly, up to 1 order of magnitude, with increasing temperature. The resulting thickness values of the Li_2O and LiF SEI were found, as anticipated, to be invariant with temperature (Figure S10), whereas conductivity exhibited strong temperature-dependence (Figure 5c). The Arrhenius plot showed a linear relationship between the reciprocal of temperature and the product of ionic conductivity and temperature in logarithmic scale, in accordance with the defect chemistry of solid-state ionic conductors.[49] The activation energy for conduction, E_a, was directly calculated from the slope of the Arrhenius relationship to be 0.58 and 0.47 eV for Li|Li_2O and Li|LiF, respectively. Additional data points for Li|Li_2O are shown in Figure S11, which shows that the activation energies for the ionic conduction of Li_2O SEI samples formed in the temperature range of 175−250 °C are similar, ranging from 0.58 to 0.63 eV as a representative range for these samples.

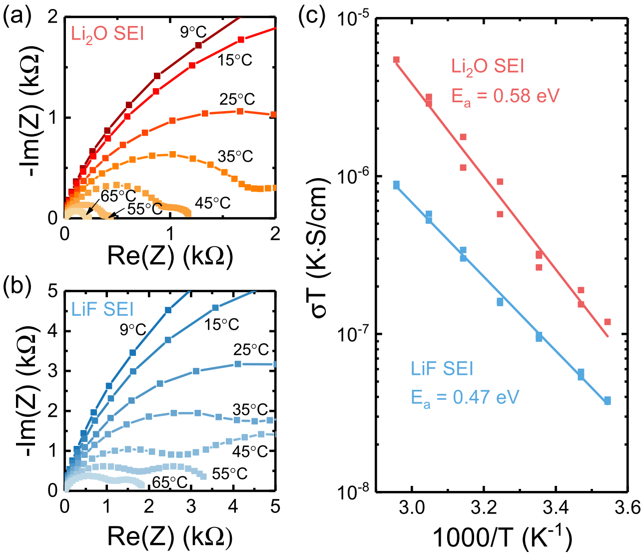

Figure 5. Nyquist plots of the EIS data of a symmetric coin cell using Li electrodes treated in (a) O_2 at 175 °C for 1 h and (b) NF_3 at 175 °C for 1 h. The temperature of the EIS measurements ranged from 9 to 65 °C. (c) Temperature dependence of the ionic conductivity of the Li_2O and LiF SEI. The activation energy E_a is calculated from the slope of the Arrhenius plot.

3.4. Discussion.

The ionic conductivities of Li_2O obtained herein, which are derived from and tested at the chemical potential of metallic Li with the electrolyte present, are significantly higher than the reported literature values of bulk counterparts: for example, $\sigma_0 \approx 10^{-12}$ S/cm for sintered pellets[21] as mentioned previously, in which the Li^+ potential within the film was estimated to be 2.8−2.9 V versus Li/Li^+.[50] Moreover, charge carrier diffusivities in Li|Li_2O ranged from $D = 10^{-9}$ to 10^{-8} cm^2/s, at least four orders of magnitude larger than that of bulk Li_2O from the same pellet measurements $(2 \times 10^{-13}$ cm^2/s).[21] We note that our obtained conductivity values show good order-of-magnitude agreement with those of a native SEI without any interfacial modification (Figure 4). Although experimental values of charge carrier concentration and diffusivity in an all-Li_2O SEI have not been reported experimentally to the best of our knowledge, our obtained values agree well with those obtained from DFT calculations of Li_2CO_3 on Li metal, with n_0 up to 1.7×10^{-7} mol/cm^3, and D as high as 1.1×10^{-7} cm^2/s[24,47] Given similar conclusions reached in studies on the Li_2CO_3 SEI,[24,47,51] it is reasonable to expect that the chemical potential of Li can promote the creation of excess Li^+ interstitials in Li_2O as well, a mechanism that is not experimentally accessible in bulk pellets. Therefore, the large differences in σ_0 and D between Li|Li_2O and sintered bulk Li_2O[21] serve as compelling evidence that more facile Li^+ transport pathways may be available when Li_2O is in contact with Li metal. Figure S12 further shows the comparison of the Arrhenius behavior of Li|Li_2O with other bulk measurements on sintered pellets measured without the presence of Li metal or electrolyte,[21,27−31] emphasizing that Li|Li_2O has significantly higher conductivity near room temperature.

In addition, significant changes were found in Li_2O transport parameters as a function of formation temperature. We attribute this to the fact that higher reaction temperatures likely support the growth of larger Li_2O grain sizes and an overall decrease in the grain boundary (defect) density. Although the transport pathways of Li^+ interstitials within the Li_2O SEI (whether through grains or grain boundaries) are currently unknown, we tentatively assign this improvement in D to arise from larger grain sizes and fewer impeding grain boundaries formed at higher reaction temperatures. The decrease in n_0 is also consistent with this picture: for Li_2O formed at higher temperature, the Li|Li_2O interface is anticipated to be more ordered with lower amounts of defects, making it more difficult to form Li^+ interstitials within the space-charge region. Overall, the increase in diffusivity, rather than the loss of carriers, with increasing reaction temperature was more significant and dominates the transport behavior, and thus the conductivity increases overall.

The conductivity of bulk LiF calculated elsewhere[48] at anodic potentials was found to be significantly lower—at approximately 10^{-31} S/cm—than observed here. However, σ_0 of LiF has been enhanced up to 6×10^{-6} S/cm by coating nanoscale LiF layers onto other substrates, creating highly disordered structures with ionic accumulation/depletion effects.[52] Therefore, it is not unreasonable to expect commensurate, relatively higher conductivity of both Li_2O and LiF when present at the metal−SEI interface with space-charge effects.

The native SEI showed over one order of magnitude higher concentration of charge carriers $(8.5 \times 10^{-6}$ mol/cm^3) than either the Li_2O or LiF SEI (1.8×10^{-7} or 2.7×10^{-7} mol/cm^3, respectively), reflective of its more disordered, multiphasic structure. Transport within an engineered multicomponent SEI with specific amounts of LiF and Li_2CO_3 was previously studied by Zhang *et al.*,[53] where the authors found that the interfaces between nanocrystalline LiF and Li_2CO_3 grains can create space-charge effects that generate an enrichment of charge carriers. This was found to improve the overall ionic conductivity in the composite SEI on the assumption of unchanged diffusivity compared to a single-component case. Our results also indicate that a more complex, native SEI will have higher charge-carrier concentrations, potentially because of the same intergrain effects, which were not present in the all-Li_2O or all-LiF model interfaces. However, we found that D of the native SEI (1.6×10^{-11} cm^2/s) was two orders of magnitude lower than the Li_2O SEI formed at room temperature (1.8×10^{-9} cm^2/s). Phases in the native SEI have been reported to be mostly amorphous with dispersed crystalline particles as revealed by recent cryo-TEM studies,[11,13] partly because the SEI is formed by rapid reactions of the Li metal and the electrolytes at room temperature under highly nonequilibrium conditions. Such a highly disordered and amorphous structure of the native SEI brings about problematic migration pathways for charge carriers, which can explain the lower D in the native SEI. A recent finding also suggests that the amorphous region in the native SEI provides slower ionic transport pathways than nanocrystalline phases.[54] Overall, the competing effects of higher n_0 and lower D led to a lower ionic conductivity for the native SEI compared to Li_2O in these experiments.

Interestingly, σ_0 of the multiphasic native SEI, at 5.1×10^{-10} S/cm, was lower than that of the Li_2O SEI but similar to LiF ($\sim 5.2 \times 10^{-10}$ S/cm). We tentatively suggest that σ_0 of the native SEI may be limited by the lower-conductivity phase, LiF, known to be omnipresent in the Li SEI because of the widespread use of fluorinated salts,[55,56] but the limiting compositions of the SEI will require further investigation in continued work when a larger range of model SEIs can be successfully synthesized and compared. Efforts to systematically vary LiF-to-Li_2O ratios and impart additional SEI-relevant, multi-component interfaces are ongoing. Broadly, our results suggest that some transport improvements may be achievable either with certain artificial interface compositions or with electrolytes engineered to enrich the SEI with Li_2O; however, the complex effects of the resulting Li_2O microstructure, which is not universal and will vary from system to system, will be critical to examine as efforts develop.

Overall, this work indicates that there is a significant opportunity to obtain more precise understanding of the SEI using experimental model systems, even regarding the simplest and most common phases such as Li_2O or LiF, about which relatively little is still known in relevant battery environments. Hopefully, better quantitative understanding of the properties and functions of individual phases in the SEI can be used in the future to guide the rational designing of electrolytes, additives, and interfaces with improved functionality for stabilizing Li.

4. CONCLUSIONS

A model interface consisting of Li_2O (20−100 nm) or LiF (∼25 nm) on Li was developed to obtain first measurements of transport properties of a single-phase SEI at the chemical potential of Li. Comprehensive EIS analysis indicated that the ionic conductivity and diffusivity of Li_2O on Li were several orders of magnitude higher than reported values obtained using bulk pellet measurements, which is attributable to the dramatically different chemical, ionic, and microstructural environments in a real SEI. The experimental values obtained with Li_2O and LiF are significantly closer to those of a native SEI and agree well with computational results. In addition, it was found that Li|Li_2O prepared herein has moderately higher conductivity than Li|LiF. Although the correspondence of our single-phase results with that of the native SEI requires continued testing in future studies to elucidate in full, these results suggest that LiF may limit transport within the SEI, and therefore that an Li_2O-rich SEI may be equally or more functional than one enriched with LiF. Overall, this work demonstrates one path forward to increase the fundamental understanding of the SEI on Li through the development of appropriate analogue interfaces that can be more readily isolated and studied than native interfaces, and which we hope will contribute to the rationalization and improvement of the SEI in future works.

■ ASSOCIATED CONTENT

Supporting Information

The Supporting Information is available free of charge at https://pubs.acs.org/doi/10.1021/acs.chemmater.0c00333.

> SEM image of Li treated in O_2; XPS depth profile of Li|Li_2O samples; Nyquist plot of the EIS data; symmetric coin cell assembled with two identical Li|Li_2O electrodes; residual impedance of a symmetric coin cell; sensitivity of EIS to transport properties; temperature-dependence of Li_2O and LiF thicknesses as well as ionic conductivity of the Li_2O SEI; and SEI thickness and Debye length (PDF)

■ AUTHOR INFORMATION

Corresponding Author

Betar M. Gallant − *Department of Mechanical Engineering, Massachusetts Institute of Technology, Cambridge, Massachusetts 02139, United States;* orcid.org/0000-0002-4586-2769; Email: bgallant@mit.edu

Author

Rui Guo − *Department of Mechanical Engineering, Massachusetts Institute of Technology, Cambridge, Massachusetts 02139, United States;* orcid.org/0000-0002-8826-2456

Complete contact information is available at:
https://pubs.acs.org/10.1021/acs.chemmater.0c00333

Notes

The authors declare no competing financial interest.

■ ACKNOWLEDGMENTS

The authors gratefully acknowledge support from the National Science Foundation under the award number 1804247. This work made use of the MRSEC Shared Experimental Facilities at MIT, supported by the National Science Foundation under the award number DMR-1419807.

■ REFERENCES

(1) Lin, D.; Liu, Y.; Cui, Y. Reviving the Lithium Metal Anode for High-Energy Batteries. *Nat. Nanotechnol.* **2017**, *12*, 194−206.

(2) Cheng, X.-B.; Zhang, R.; Zhao, C.-Z.; Zhang, Q. Toward Safe Lithium Metal Anode in Rechargeable Batteries: A Review. *Chem. Rev.* **2017**, *117*, 10403−10473.

(3) Fang, C.; Li, J.; Zhang, M.; Zhang, Y.; Yang, F.; Lee, J. Z.; Lee, M.-H.; Alvarado, J.; Schroeder, M. A.; Yang, Y.; Lu, B.; Williams, N.; Ceja, M.; Yang, L.; Cai, M.; Gu, J.; Xu, K.; Wang, X.; Meng, Y. S. Quantifying Inactive Lithium in Lithium Metal Batteries. *Nature* **2019**, *572*, 511−515.

(4) Aurbach, D.; Zinigrad, E.; Cohen, Y.; Teller, H. A Short Review of Failure Mechanisms of Lithium Metal and Lithiated Graphite Anodes in Liquid Electrolyte Solutions. *Solid State Ionics* **2002**, *148*, 405−416.

(5) Wood, K. N.; Kazyak, E.; Chadwick, A. F.; Chen, K.-H.; Zhang, J.-G.; Thornton, K.; Dasgupta, N. P. Dendrites and Pits: Untangling the Complex Behavior of Lithium Metal Anodes through Operando Video Microscopy. *ACS Cent. Sci.* **2016**, *2*, 790−801.

(6) Shi, F.; Pei, A.; Vailionis, A.; Xie, J.; Liu, B.; Zhao, J.; Gong, Y.; Cui, Y. Strong Texturing of Lithium Metal in Batteries. *Proc. Natl. Acad. Sci. U.S.A.* **2017**, *114*, 12138−12143.

(7) Tikekar, M. D.; Choudhury, S.; Tu, Z. Y.; Archer, L. A. Design Principles for Electrolytes and Interfaces for Stable Lithium-Metal Batteries. *Nat. Energy* **2016**, *1*, 16114.

(8) Peled, E.; Menkin, S. Review-SEI: Past, Present and Future. *J. Electrochem. Soc.* **2017**, *164*, A1703−A1719.

(9) Schechter, A.; Aurbach, D.; Cohen, H. X-Ray Photoelectron Spectroscopy Study of Surface Films Formed on Li Electrodes Freshly Prepared in Alkyl Carbonate Solutions. *Langmuir* **1999**, *15*, 3334−3342.

(10) Suo, L.; Xue, W.; Gobet, M.; Greenbaum, S. G.; Wang, C.; Chen, Y.; Yang, W.; Li, Y.; Li, J. Fluorine-Donating Electrolytes Enable Highly Reversible 5-V-Class Li Metal Batteries. *Proc. Natl. Acad. Sci. U.S.A.* **2018**, *115*, 1156−1161.

(11) Liu, Y.; Lin, D.; Li, Y.; Chen, G.; Pei, A.; Nix, O.; Li, Y.; Cui, Y. Solubility-Mediated Sustained Release Enabling Nitrate Additive in Carbonate Electrolytes for Stable Lithium Metal Anode. *Nat. Commun.* **2018**, *9*, 3656.

(12) Genovese, M.; Louli, A. J.; Weber, R.; Sanderson, R. J.; Johnson, M. B.; Dahn, J. R. Combinatorial Methods for Improving Lithium Metal Cycling Efficiency. *J. Electrochem. Soc.* **2018**, *165*, A3000−A3013.

(13) Li, Y.; Li, Y.; Pei, A.; Yan, K.; Sun, Y.; Wu, C.-L.; Joubert, L.-M.; Chin, R.; Koh, A. L.; Yu, Y.; Perrino, J.; Butz, B.; Chu, S.; Cui, Y. Atomic Structure of Sensitive Battery Materials and Interfaces Revealed by Cryo-Electron Microscopy. *Science* **2017**, *358*, 506−510.

(14) Li, Y.; Sun, Y.; Pei, A.; Chen, K.; Vailionis, A.; Li, Y.; Zheng, G.; Sun, J.; Cui, Y. Robust Pinhole-Free Li_3N Solid Electrolyte Grown from Molten Lithium. *ACS Cent. Sci.* **2018**, *4*, 97−104.

(15) Cha, E.; Patel, M. D.; Park, J.; Hwang, J.; Prasad, V.; Cho, K.; Choi, W. 2D MoS_2 as an Efficient Protective Layer for Lithium Metal Anodes in High-Performance Li-S Batteries. *Nat. Nanotechnol.* **2018**, *13*, 337−344.

(16) Zhao, J.; Liao, L.; Shi, F.; Lei, T.; Chen, G.; Pei, A.; Sun, J.; Yan, K.; Zhou, G.; Xie, J.; Liu, C.; Li, Y.; Liang, Z.; Bao, Z.; Cui, Y. Surface Fluorination of Reactive Battery Anode Materials for Enhanced Stability. *J. Am. Chem. Soc.* **2017**, *139*, 11550−11558.

(17) Kozen, A. C.; Lin, C.-F.; Pearse, A. J.; Schroeder, M. A.; Han, X.; Hu, L.; Lee, S.-B.; Rubloff, G. W.; Noked, M. Next-Generation Lithium Metal Anode Engineering via Atomic Layer Deposition. *ACS Nano* **2015**, *9*, 5884−5892.

(18) Chen, L.; Chen, K.-S.; Chen, X.; Ramirez, G.; Huang, Z.; Geise, N. R.; Steinrück, H.-G.; Fisher, B. L.; Shahbazian-Yassar, R.; Toney, M. F.; Hersam, M. C.; Elam, J. W. Novel ALD Chemistry Enabled Low-Temperature Synthesis of Lithium Fluoride Coatings for Durable Lithium Anodes. *ACS Appl. Mater. Interfaces* **2018**, *10*, 26972−26981.

(19) Chen, Y. C.; Ouyang, C. Y.; Song, L. J.; Sun, Z. L. Electrical and Lithium Ion Dynamics in Three Main Components of Solid Electrolyte Interphase from Density Functional Theory Study. *J. Phys. Chem. C* **2011**, *115*, 7044−7049.

(20) Benitez, L.; Seminario, J. M. Ion Diffusivity through the Solid Electrolyte Interphase in Lithium-Ion Batteries. *J. Electrochem. Soc.* **2017**, *164*, E3159−E3170.

(21) Lorger, S.; Usiskin, R.; Maier, J. Transport and Charge Carrier Chemistry in Lithium Oxide. *J. Electrochem. Soc.* **2019**, *166*, A2215−A2220.

(22) Ramasubramanian, A.; Yurkiv, V.; Foroozan, T.; Ragone, M.; Shahbazian-Yassar, R.; Mashayek, F. Lithium Diffusion Mechanism through Solid−Electrolyte Interphase in Rechargeable Lithium Batteries. *J. Phys. Chem. C* **2019**, *123*, 10237−10245.

(23) Peled, E.; Golodnitsky, D.; Ardel, G. Advanced Model for Solid Electrolyte Interphase Electrodes in Liquid and Polymer Electrolytes. *J. Electrochem. Soc.* **1997**, *144*, L208−L210.

(24) Shi, S.; Qi, Y.; Li, H.; Hector, L. G. Defect Thermodynamics and Diffusion Mechanisms in Li_2CO_3 and Implications for the Solid Electrolyte Interphase in Li-Ion Batteries. *J. Phys. Chem. C* **2013**, *117*, 8579−8593.

(25) Yildirim, H.; Kinaci, A.; Chan, M. K. Y.; Greeley, J. P. First-Principles Analysis of Defect Thermodynamics and Ion Transport in Inorganic SEI Compounds: LiF and NaF. *ACS Appl. Mater. Interfaces* **2015**, *7*, 18985−18996.

(26) Kamphaus, E. P.; Angarita-Gomez, S.; Qin, X.; Shao, M.; Engelhard, M.; Mueller, K. T.; Murugesan, V.; Balbuena, P. B. Role of Inorganic Surface Layer on Solid Electrolyte Interphase Evolution at Li-Metal Anodes. *ACS Appl. Mater. Interfaces* **2019**, *11*, 31467−31476.

(27) Huggins, R. A. Recent Results on Lithium Ion Conductors. *Electrochim. Acta* **1977**, *22*, 773−781.

(28) Biefeld, R. M.; Johnson, R. Ionic Conductivity of Li_2O-Based Mixed Oxides and the Effects of Moisture and LiOH on Their Electrical and Structural Properties. *J. Electrochem. Soc.* **1979**, *126*, 1−6.

(29) Mousa, M.; Oei, Y. S.; Richtering, H. Nmr Investigations of Cation Diffusion in Some Solids with Antifluorite Structure. *J. Phys. Colloq.* **1980**, *41*, C6.

(30) Ohno, H.; Konishi, S.; Noda, K.; Takeshita, H.; Yoshida, H.; Watanabe, H.; Matsuo, T. Conductivities of a Sintered Pellet and a Single Crystal of Li_2O. *J. Nucl. Mater.* **1983**, *118*, 242−247.

(31) Chadwick, A. V.; Flack, K. W.; Strange, J. H.; Harding, J. Defect Structures and Ionic Transport in Lithium Oxide. *Solid State Ionics* **1988**, *28−30*, 185−188.

(32) Indris, S.; Heitjans, P.; Roman, H. E.; Bunde, A. Nanocrystalline Versus Microcrystalline Li_2O:B_2O_3 Composites: Anomalous Ionic Conductivities and Percolation Theory. *Phys. Rev. Lett.* **2000**, *84*, 2889.

(33) Churikov, A. V.; Gamayunova, I. M.; Shirokov, A. V. Ionic Processes in Solid-Electrolyte Passivating Films on Lithium. *J. Solid State Electrochem.* **2000**, *4*, 216−224.

(34) Churikov, A. V.; Nimon, E. S.; Lvov, A. L. Impedance of Li-Sn, Li-Cd and Li-Sn-Cd Alloys in Propylene Carbonate Solution. *Electrochim. Acta* **1997**, *42*, 179−189.

(35) He, M.; Guo, R.; Hobold, G. M.; Gao, H.; Gallant, B. M. The Intrinsic Behavior of Lithium Fluoride in Solid Electrolyte Interphases on Lithium. *Proc. Natl. Acad. Sci. U.S.A.* **2020**, *117*, 73−79.

(36) Barr, T. L.; Seal, S. Nature of the Use of Adventitious Carbon as a Binding-Energy Standard. *J. Vac. Sci. Technol., A* **1995**, *13*, 1239−1246.

(37) David, D. J.; Froning, M. H.; Wittberg, T. N.; Moddeman, W. E. Surface Reactions of Lithium with the Environment. *Appl. Surf. Sci.* **1981**, *7*, 185−195.

(38) Zavadil, K. R.; Armstrong, N. R. Surface Chemistries of Lithium: Detailed Characterization of the Reactions with O_2 and H_2O Using XPS, EELS, and Microgravimetry. *Surf. Sci.* **1990**, *230*, 47−60.

(39) Li, Y.; Li, Y.; Sun, Y.; Butz, B.; Yan, K.; Koh, A. L.; Zhao, J.; Pei, A.; Cui, Y. Revealing Nanoscale Passivation and Corrosion Mechanisms of Reactive Battery Materials in Gas Environments. *Nano Lett.* **2017**, *17*, 5171−5178.

(40) Wood, K. N.; Teeter, G. XPS on Li-Battery-Related Compounds: Analysis of Inorganic SEI Phases and a Methodology for Charge Correction. *ACS Appl. Energy Mater.* **2018**, *1*, 4493−4504.

(41) Thevenin, J. Passivating Films on Lithium Electrodes - an Approach by Means of Electrode Impedance Spectroscopy. *J. Power Sources* **1985**, *14*, 45−52.
(42) Aurbach, D.; Zaban, A.; Gofer, Y.; Abramson, O.; Benzion, M. Studies of Li Anodes in the Electrolyte System 2Me-THF/THF/Me-Furan/$LiAsF_6$. *J. Electrochem. Soc.* **1995**, *142*, 687−696.
(43) Moshtev, R. V.; Puresheva, B. AC Impedance Study of the Lithum Electrode in Propylene Carbonate Solutions: Part I. Effect of the Surface Preparation on the Initial Impedance Parameters. *J. Electroanal. Chem.* **1984**, *180*, 609−617.
(44) Zaban, A.; Zinigrad, E.; Aurbach, D. Impedance Spectroscopy of Li Electrodes. 4. A General Simple Model of the Li-Solution Interphase in Polar Aprotic Systems. *J. Phys. Chem.* **1996**, *100*, 3089−3101.
(45) Aurbach, D. Review of Selected Electrode−Solution Interactions Which Determine the Performance of Li and Li Ion Batteries. *J. Power Sources* **2000**, *89*, 206−218.
(46) Andeen, C.; Fontanella, J.; Schuele, D. Low-Frequency Dielectric Constant of LiF, NaF, NaCl, NaBr, KCl, and KBr by the Method of Substitution. *Phys. Rev. B: Solid State* **1970**, *2*, 5068.
(47) Shi, S.; Lu, P.; Liu, Z.; Qi, Y.; Hector, L. G.; Li, H.; Harris, S. J. Direct Calculation of Li-Ion Transport in the Solid Electrolyte Interphase. *J. Am. Chem. Soc.* **2012**, *134*, 15476−15487.
(48) Pan, J.; Cheng, Y. T.; Qi, Y. General Method to Predict Voltage-Dependent Ionic Conduction in a Solid Electrolyte Coating on Electrodes. *Phys. Rev. B: Condens. Matter Mater. Phys.* **2015**, *91*, 134116.
(49) Smyth, D. M. *The Defect Chemistry of Metal Oxides*; Oxford University Press, 2000.
(50) Lau, K. C.; Curtiss, L. A.; Greeley, J. Density Functional Investigation of the Thermodynamic Stability of Lithium Oxide Bulk Crystalline Structures as a Function of Oxygen Pressure. *J. Phys. Chem. C* **2011**, *115*, 23625−23633.
(51) Islam, M. M.; Bredow, T.; Minot, C. Theoretical Analysis of Structural, Energetic, Electronic, and Defect Properties of Li_2O. *J. Phys. Chem. B* **2006**, *110*, 9413−9420.
(52) Li, C.; Gu, L.; Maier, J. Enhancement of the Li Conductivity in LiF by Introducing Glass/Crystal Interfaces. *Adv. Funct. Mater.* **2012**, *22*, 1145−1149.
(53) Zhang, Q.; Pan, J.; Lu, P.; Liu, Z.; Verbrugge, M. W.; Sheldon, B. W.; Cheng, Y.-T.; Qi, Y.; Xiao, X. Synergetic Effects of Inorganic Components in Solid Electrolyte Interphase on High Cycle Efficiency of Lithium Ion Batteries. *Nano Lett.* **2016**, *16*, 2011−2016.
(54) Li, Y.; Huang, W.; Li, Y.; Pei, A.; Boyle, D. T.; Cui, Y. Correlating Structure and Function of Battery Interphases at Atomic Resolution Using Cryoelectron Microscopy. *Joule* **2018**, *2*, 2167−2177.
(55) Aurbach, D.; Daroux, M.; McDougall, G.; Yeager, E. B. Spectroscopic Studies of Lithium in an Ultrahigh Vacuum System. *J. Electroanal. Chem.* **1993**, *358*, 63−76.
(56) Kanamura, K.; Tamura, H.; Shiraishi, S.; Takehara, Z. i. XPS Analysis of Lithium Surfaces Following Immersion in Various Solvents Containing $LiBF_4$. *J. Electrochem. Soc.* **1995**, *142*, 340−347.